PCCP

PAPER

View Article Online
View Journal | View Issue

Cite this: *Phys. Chem. Chem. Phys.*, 2018, **20**, 28425

Inelastic vibrational dynamics of CS in collision with H_2 using a full-dimensional potential energy surface†

Benhui Yang, *[a] P. Zhang,[b] C. Qu,[c] P. C. Stancil,[a] J. M. Bowman,[c] N. Balakrishnan[d] and R. C. Forrey[e]

Received 14th September 2018,
Accepted 30th October 2018

DOI: 10.1039/c8cp05819a

rsc.li/pccp

We report a six-dimensional (6D) potential energy surface (PES) for the CS–H_2 system computed using high-level electronic structure theory and fitted using a hybrid invariant polynomial method. Full-dimensional quantum close-coupling scattering calculations have been carried out using this potential for rotational and, for the first time, vibrational quenching transitions of CS induced by H_2. State-to-state cross sections and rate coefficients for rotational transitions in CS from rotational levels j_1 = 0–5 in the ground vibrational state are compared with previous theoretical results obtained using a rigid-rotor approximation. For vibrational quenching, state-to-state and total cross sections and rate coefficients were calculated for the vibrational transitions in CS(v_1 = 1,j_1) + H_2(v_2 = 0,j_2) → CS(v_1' = 0,j_1') + H_2(v_2' = 0,j_2') collisions, for j_1 = 0–5. Cross sections for collision energies in the range 1 to 3000 cm^{-1} and rate coefficients in the temperature range of 5 to 600 K are obtained for both *para*-H_2 (j_2 = 0) and *ortho*-H_2 (j_2 = 1) collision partners. Application of the computed results in astrophysics is also discussed.

1 Introduction

Quantum mechanical calculations of molecular scattering are of great interest for chemical dynamics and astrophysics studies.[1] Carbon monosulfide (CS), the sulfur analogue of carbon monoxide, was first detected by Penzias *et al.*[2] through the line emission of J = 3–2 in four sources including Orion A, W51, IRC + 10216, and DR 21. It is also the first sulfur-containing molecule observed in interstellar space. Since then numerous observations of CS have been reported[3–10] in a variety interstellar regions. Observations of the CS emission lines are very useful for investigation of the molecular gas and its composition. An accurate prediction of the abundance of CS in the interstellar medium requires its collisional rate coefficients with ambient species. So far available collisional rate coefficients are limited to rigid-rotor calculations for a small range of rotational transitions in the vibrational ground state.[11–14] In interstellar clouds, molecular hydrogen is the most abundant species and the dominant collision partner. Therefore, the vibrational and rotational rate coefficients of CS by H_2 impact is of great importance in astrophysics, astrochemistry, and in interstellar regions where non-equilibrium process plays a dominant role. In particular, with the detection of CS in vibrationally excited states, the rovibrational rate coefficients are needed to analyze CS lines and model the emission and thermal balance in the interstellar medium.

Due to its astrophysical importance, there have been many theoretical studies of pure rotational cross sections and rate coefficients for CS in collision with H_2. Green and Chapman[11] calculated CS–H_2 rotational excitation rate coefficients among first 13 rotational states of CS. Later Turner *et al.*[12] extended the calculations to rotational levels through j_1 = 20 for rate coefficient below 300 K. However these rate coefficients were computed using a CS–He PES obtained from an electron gas model.[15] Vastel *et al.*[10] performed local thermodynamic equilibrium (LTE) and non-LTE radiative transfer modeling using the NAUTILUS chemical code for the sulfur chemistry in the L1544 pre-stellar core; the rate coefficients of CS with *para*-H_2 calculated by Green and Chapman[11] were adopted to obtain the column density of CS. Albrecht presented approximate rate coefficients for CS–H_2 (j_2 = 0) using an empirical analytical expression[16] and a fit to the rate coefficients of Green and Chapman.[11] This approximation was also adopted to derive the collisional rate coefficients of linear molecules SiO, HCN, H_2O.[17,18] Recently, a four-dimensional (4D)

[a] *Department of Physics and Astronomy and Center for Simulational Physics, University of Georgia, Athens, GA 30602, USA. E-mail: yang@physast.uga.edu*
[b] *Department of Chemistry, Duke University, Durham, NC 27708, USA*
[c] *Department of Chemistry, Emory University, Atlanta, GA 30322, USA*
[d] *Department of Chemistry and Biochemistry, University of Nevada, Las Vegas, NV 89154, USA*
[e] *Department of Physics, Penn State University, Berks Campus, Reading, PA 19610, USA*

† Electronic supplementary information (ESI) available: The potential energy surface subroutine. See DOI: 10.1039/c8cp05819a

potential energy surface (PES) for CS–H_2 was constructed by Denis-Alpizar *et al.*[20] based on *ab initio* calculations within the coupled-cluster singles and doubles plus perturbative triples[CCSD(T)] method and the augmented correlation consistent polarized valence quadruple zeta (aug-cc-pVQZ) basis set. The interaction energy between CS and H_2 was obtained by subtracting the sum of the monomer potentials of CS and H_2 from the total energy of the CS–H_2 complex, where CS and H_2 were treated as rigid rotors with the bond length of H_2 fixed at its vibrationally averaged value, $r_0 = 1.4467a_0$ in the vibrational ground state and the bond length of CS fixed at its equilibrium value ($r_e = 2.9006a_0$). The PES was fitted with a least squares procedure for the angular terms and interpolation of the radial coefficients with cubic splines.[19] This 4D rigid rotor PES was applied to compute the rotational (de)excitation rate coefficients for the first 30 rotational levels of CS by collision with *para*-H_2 ($j_2 = 0$) and *ortho*-H_2 ($j_2 = 1$).[13,14] Additionally, the CS–*para*-H_2 rate coefficients obtained by mass-scaling the CS–He results of Lique *et al.*[21] are also available in the Leiden Atomic and Molecular Database.[23] These scaled results were also adopted by Neufeld *et al.*[8] in their turbulent dissipation region models to determine the equilibrium level populations of CS in diffuse molecular clouds, where CS $j_1 = 2$–1 line was observed using the IRAM 30 m telescope. For CS vibrational excitation, Lique and Spielfiedel[22] performed the scattering calculations of rovibrational excitation cross sections and rate coefficients of CS by He. However, to our knowledge, there are no theoretical results available for vibrational excitation of CS with H_2. The only available measurements are for the removal rate constants for vibrationally excited CS($v_1 = 1$) with H_2, reported about a half century ago.[24,25]

Quantum close-coupling (CC) calculations are the primary source of rate coefficients for astrophysical modeling. Full-dimensional quantum CC formalism has been developed[26,27] for collisions involving two diatomic molecules. With the development of the quantum CC scattering code TwoBC,[28] diatom–diatom systems in full-dimensionality can be treated and was first used for CC calculations of rovibrational collisions of H_2 with H_2.[29–32] Rovibrational CC calculations were also performed for the collisional systems CO–H_2,[33,34] CN–H_2,[35] SiO–H_2,[36] along with coupled-states approximation calculations in 5D and 6D.[37–39]

Here we report the first full-dimensional PES and the first vibrational inelastic scattering calculations for the CS–H_2 system. The paper is organized as follows. A brief description of the Theoretical methods for the electronic structure and scattering calculations are given in Section 2. The results are presented and discussed in Section 3 followed by Astrophysical applications in Section 4. Section 5 summarizes the results and presents an outlook on future work.

2 Theoretical methods

We briefly describe in this section the theoretical methods applied in the computation and analytical fit of the CS–H_2 PES as well as the quantum CC calculations in full dimensionality. The reader is referred to ref. 30, 33 and 40 for the details of the theoretical methodology.

2.1 Potential energy surface computation and fit

The interaction potential of CS–H_2 in the electronic ground state was computed on a 6D grid using Jacobi coordinates (R,r_1,r_2,θ_1,θ_2,ϕ). As shown in Fig. 1, R denotes the distance between the centers of mass of CS and H_2, and r_1 and r_2 are the bond lengths describing the vibration of CS and H_2, respectively. The angles θ_1 and θ_2, respectively, are the in-plane orientation angles of $\vec{r}_1$ and $\vec{r}_2$ with $\vec{R}$, while ϕ denotes the out-of-plane dihedral angle. The PES was computed with the MOLPRO suite of computational chemistry codes.[41,42] The intermolecular distance R was chosen in the range of 4.5–25a_0 and the bond distances are confined to $2.55 \leq r_1 \leq 3.51a_0$ and $1.05 \leq r_2 \leq 2.27a_0$. Here $a_0 = 0.529$ Å is the Bohr radius. To produce an accurate 6D PES with proper symmetry the *ab initio* calculations were performed over the angular coordinates $0 \leq \theta_1 \leq 360^\circ$ and $0 \leq \theta_2, \phi \leq 180^\circ$, where $\theta_1 = \theta_2 = 0^\circ$ corresponds to the collinear configuration C–S–H–H.

The *ab initio* electronic structure computations of potential energies were performed using the explicitly correlated coupled-cluster (CCSD(T)-F12b) method.[43,44] All the calculations employed aug-cc-pV5Z (for H and C atoms)[45] and aug-cc-pV(5+d)Z (for S atom) orbital basis set,[46] and the corresponding MP2FIT (for H and C atoms) and aug-cc-pwCV5Z (for S atom) auxiliary bases[47,48] for density fitting. The aug-cc-pV6Z-RI auxiliary bases (without k functions)[49] were used for the resolutions of the identify and density-fitted Fock matrices for all orbital bases. No scaled triples correction was used in the CCSD(T)-F12 calculation. The interaction PES was corrected for basis set superposition error (BSSE)[50] using the counter-poise (CP)[51] method. Benchmark calculations at this CCSD(T)-F12 level were carried out on selected molecular configurations and results were compared with those from the conventional CCSD(T) method using aug-cc-pV5Z. The CP corrected interaction energy agrees closely with those derived from CCSD(T)/aug-cc-pV5Z.

The full-dimensional CS–H_2 interaction potential, referred to as VCSH2, is a hybrid one combining a fit to the full *ab initio* data set (denoted V_I) and a fit to the long-range data (denoted V_{II}) and is expressed by

$$V = (1 - s)V_I + sV_{II}, \quad (1)$$

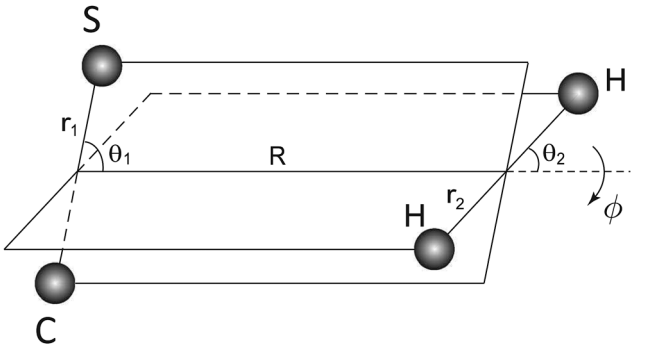

Fig. 1 The six-dimensional Jacobi coordinates for the CS–H_2 system.

the switching function s is given as

$$s = \begin{cases} 0 & (R < R_i) \\ 10b^3 - 15b^4 + 6b^5 & (R_i < R < R_f), \\ 1 & (R > R_f) \end{cases} \quad (2)$$

where $b = (R - R_i)/(R_f - R_i)$, $R_i = 8.5a_0$ and $R_f = 10.5a_0$ are the lower and upper bound of the switching region, respectively. Both V_I and V_{II} are expanded in the form

$$V_{I,II}(y_1 \cdots y_6) = \sum_{n_1 \cdots n_6} C_{n_1 \cdots n_6} y_1^{n_1} y_6^{n_6} \left(y_2^{n_2} y_3^{n_3} y_4^{n_4} y_5^{n_5} + y_2^{n_3} y_3^{n_2} y_4^{n_5} y_5^{n_4} \right) \quad (3)$$

and have been fitted in 6D using an invariant polynomial method,[40,52] where $y_i = \exp(-d_i/p)$ are Morse-type variables and p is a user-specified parameter with $p = 2.0a_0$ for V_I and $p = 7.0a_0$ for V_{II}. The parameters d_i are the internuclear distances between two atoms and defined as $d_1 = d_{CS}$, $d_2 = d_{CH}$, $d_3 = d_{CH}$, $d_4 = d_{SH}$, $d_5 = d_{SH}$ and $d_6 = d_{HH}$. The powers $n_1, \cdots, n_6$ satisfy $n_1 + \cdots + n_6 \leq 7$ and $n_2 + n_3 + n_4 + n_5 \neq 0$, and the interaction potential is guaranteed to approach zero when CS and H_2 are infinitely far apart for all r_1 and r_2. The total number of fitted linear coefficients $C_{n1 \cdots n6}$ is 882, and these coefficients were determined *via* linear least-squares fitting using the software MSA.[53] The root mean square (RMS) error in the long range fit V_{II} is 0.062 cm^{-1}, for V_I the RMS error is 14.2 cm^{-1}.

In Fig. 2 the R dependence of VCSH2 PES is compared with the PES of Denis-Alpizar *et al.*[20] for $(\theta_1, \theta_2, \phi) = (0°, 0°, 0°)$, $(180°, 0°, 0°)$, $(180°, 90°, 0°)$, and $(90°, 90°, 90°)$. Good agreement between our PES and the PES of Denis-Alpizar *et al.*[20] is displayed, except that our PES is a little shallower at the global minimum. Our fitted PES has a depth of -162.56 cm^{-1} at the collinear structure with the C atom towards to H_2 and $R = 8.6a_0$. The minimum of the PES of Denis-Alpizar *et al.*[20] is about -173 cm^{-1} and also corresponds to a collinear geometry with same R value.

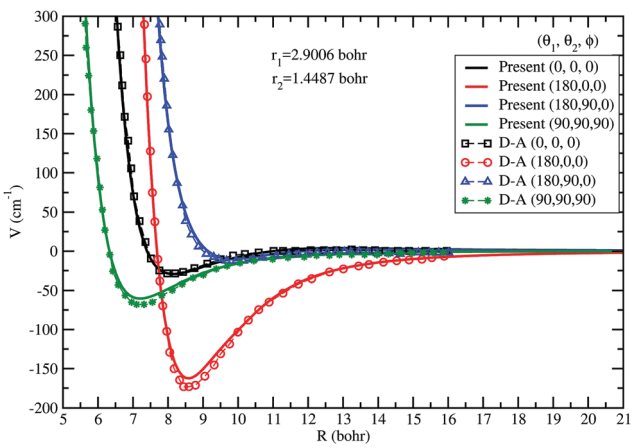

Fig. 2 The R dependence of the CS–H_2 interaction potential, VCSH2 for $(\theta_1, \theta_2, \phi) = (0°, 0°, 0°)$, $(180°, 90°, 0°)$, $(90°, 90°, 90°)$, and $(180°, 0°, 0°)$. The bond lengths of CS and H_2 are fixed at equilibrium value and vibrationally averaged value in the rovibrational ground state, respectively. Symbols are for the PES of Denis-Alpizar *et al.*[20] (D–A).

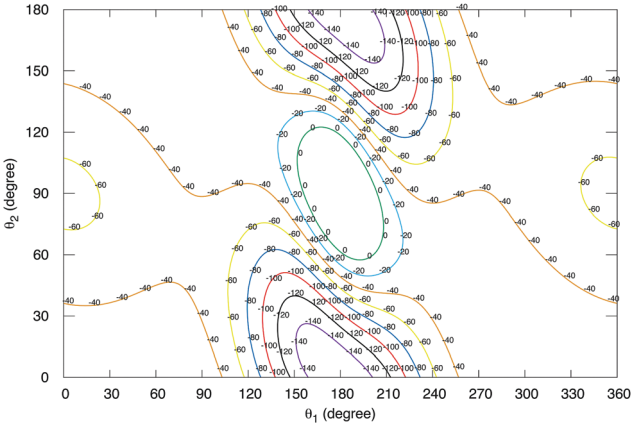

Fig. 3 Contour plots of the potential VCSH2 as a function of θ_1 and θ_2 for $r_1 = 2.9006a_0$, $r_2 = 1.4011a_0$, $R = 8.5a_0$, and $\phi = 0°$.

Fig. 3 shows a two-dimensional contour plot of the VCSH2 PES in θ_1, θ_2 space for fixed values of $r_1 = 2.9006a_0$, $r_2 = 1.4011a_0$, $R = 8.5a_0$, and $\phi = 0°$.

2.2 Scattering calculation

The full-dimensional quantum CC scattering calculations were performed using the TwoBC code.[28] To facilitate the scattering calculations, it is convenient to expand the angular dependence of the interaction potential between CS and H_2, $V(\vec{r}_1, \vec{r}_2, \vec{R})$ at each intermolecular distance R according to,[54]

$$V(R, r_1, r_2, \theta_1, \theta_2, \phi) = \sum_{\lambda_1 \lambda_2 \lambda_{12}} A_{\lambda_1 \lambda_2 \lambda_{12}}(r_1, r_2, R) Y_{\lambda_1 \lambda_2 \lambda_{12}}(\hat{r}_1, \hat{r}_2, \hat{R}), \quad (4)$$

where the bi-spherical harmonic function is expressed as,

$$Y_{\lambda_1 \lambda_2 \lambda_{12}}(\hat{r}_1, \hat{r}_2, \hat{R}) = \sum_{m_{\lambda_1} m_{\lambda_2} m_{\lambda_{12}}} \langle \lambda_1 m_{\lambda_1} \lambda_2 m_{\lambda_2} | \lambda_{12} m_{\lambda_{12}} \rangle \times Y_{\lambda_1 m_{\lambda_1}}(\hat{r}_1) Y_{\lambda_2 m_{\lambda_2}}(\hat{r}_2) Y^*_{\lambda_{12} m_{\lambda_{12}}}(\hat{R}). \quad (5)$$

Terms $0 \leq \lambda_1 \leq 8$ and $0 \leq \lambda_2 \leq 4$ are retained in the expansion. Only even values of λ_2 contribute because H_2 is homonuclear.

We use a combined molecular state (CMS)[30] notation, $(v_1 j_1 v_2 j_2)$, to describe a combination of rovibrational states for CS$(v_1 j_1)$ and $H_2(v_2 j_2)$, where j_i and v_i $(i = 1, 2)$ are the rotational and vibrational quantum numbers of CS and H_2. For a rovibrational transition the state-to-state cross section can be obtained as a function of the collision energy E_c from the corresponding scattering matrix S:

$$\sigma_{v_1 j_1 v_2 j_2 \to v_1' j_1' v_2' j_2'}(E_c) = \frac{\pi}{(2j_1 + 1)(2j_2 + 1)k^2} \times \sum_{j_{12} j_{12}' l l' J \varepsilon_I} (2J + 1) \left| \delta_{v_1 j_1 v_2 j_2, v_1' j_1' v_2' j_2'} - S^{J \varepsilon_I}_{v_1 j_1 v_2 j_2 l, v_1' j_1' v_2' j_2' l'}(E_c) \right|^2, \quad (6)$$

where the wave vector $k = \sqrt{2\mu E_c/\hbar^2}$ and the primed quantities refer to the final state. The quantum number J denotes the total angular momentum, $\vec{J} = \vec{l} + \vec{j}_{12}$, with $\vec{j}_{12} = \vec{j}_1 + \vec{j}_2$ and l is the orbital angular momentum quantum number.

The total quenching cross section of CS from initial state $(v_1 j_1 v_2 j_2) \rightarrow (v_1'; v_2' j_2')$ is obtained by summing the state-to-state quenching cross sections over the final rotational state of j_1' of CS in vibrational state v_1',

$$\sigma_{v_1 j_1 v_2 j_2 \rightarrow v_1'; v_2' j_2'}(E_c) = \sum_{j_1'} \sigma_{v_1 j_1 v_2 j_2 \rightarrow v_1' j_1' v_2' j_2'}(E_c). \quad (7)$$

From the state-to-state cross section $\sigma_{v_1 j_1 v_2 j_2 \rightarrow v_1' j_1' v_2' j_2'}$ the corresponding rate coefficient at a temperature T can be obtained by averaging it over a Boltzmann distribution of collision energies.

$$k_{v_1 j_1 v_2 j_2 \rightarrow v_1' j_1' v_2' j_2'}(T) = \left(\frac{8}{\pi\mu\beta}\right)^{1/2} \beta^2 \times \int_0^\infty E_c \sigma_{v_1 j_1 v_2 j_2 \rightarrow v_1' j_1' v_2' j_2'}(E_c) \exp(-\beta E_c) \mathrm{d}E_c, \quad (8)$$

where μ is the reduced mass of the CS–H_2 system, $\beta = (k_B T)^{-1}$, and k_B is Boltzmann's constant.

In the full-dimensional rovibrational scattering calculations with the TwoBC code[28] the log-derivative matrix propagation method of Johnson[55] was employed to propagate the CC equations from $R = 4.5a_0$ to $25a_0$. The number of Gauss–Hermite quadrature points N_{r_1}, N_{r_2}; the number of Gauss–Legendre quadrature points in θ_1 and θ_2, N_{θ_1}, N_{θ_2}; and the number of Chebyshev quadrature points in ϕ, N_ϕ adopted to project out the expansion coefficients of the PES are listed in Table 1. In the scattering calculations, the monomer potentials of Paulose *et al.*[56] and Schwenke[57] are used to describe the rovibrational motions of CS and H_2, respectively.

3 Results and discussion

3.1 Pure rotational de-excitation

The rotational de-excitation cross sections of CS($v_1 = 0$, j_1) in collision with H_2 have been calculated for the transitions, CS($v_1 = 0, j_1$) + H_2($v_2 = 0, j_2$) → CS($v_1' = 0, j_1'$) + H_2($v_2' = 0, j_2'$), where both CS and H_2 are taken to be in their ground vibrational states, *i.e.*, $(0 j_1 0 j_2) \rightarrow (0 j_1' 0 j_2')$. We performed the calculations in full-dimension for the initial rotational states of CS j_1 = 1–5, with collision energy ranging from 1 to 3000 cm^{-1}. Sufficient number of partial waves were included to ensure the convergence of the cross sections. Convergence tests were also made with respect to the *para*-H_2 basis, it was found that the effect from inclusion of the $j_2 = 4$ state is generally less than 1%. The basis sets and partial waves used in the scattering calculations are provided in Table 1. In Fig. 4 the state-to-state quenching cross sections of CS from initial state $j_1 = 5$ from our calculations are compared with the results of Denis-Alpizar *et al.*[13] Results are presented for both *para*-H_2 ($j_2 = 0$) and *ortho*-H_2 ($j_2 = 1$) for final states $j_1' = 0$, 1, 2, 3, and 4. Fig. 4(a) shows that for *para*-H_2, for collision energies below ~30 cm^{-1}, all state-to-state cross sections display resonances due to the decay of quasibound states supported by the van der Waals well of the PES. At collision energies below 200 cm^{-1}, the cross sections generally increase with increasing j_1' with the smallest cross section

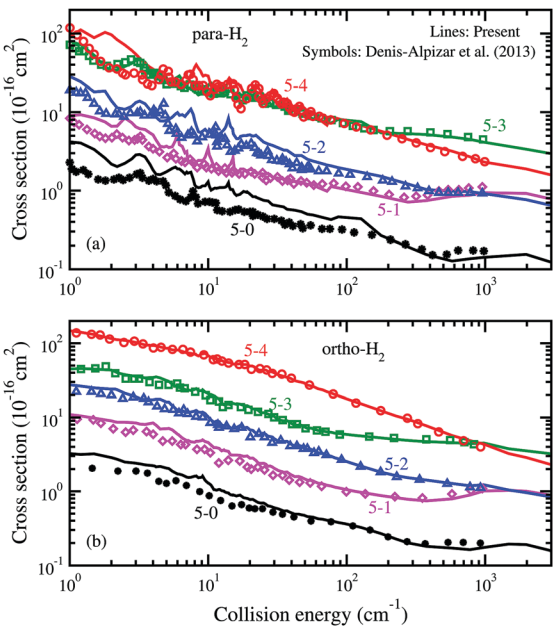

Fig. 4 Rotational state-to-state de-excitation cross sections for CS(j_1) + H_2(j_2) → CS(j_1') + H_2(j_2'), $j_1 = 5$, $j_1' < j_1$. Lines are for the present results and symbols are for the results of Denis-Alpizar *et al.*[13] (a) CS in collision with *para*-H_2, $j_2 = j_2' = 0$; (b) CS in collision with *ortho*-H_2, $j_2 = j_2' = 1$.

Table 1 Parameters used in the scattering calculations

	Basis set	$N_{\theta_1}(N_{\theta_2})$	N_ϕ	$N_{r_1}(N_{r_2})$	λ_1	λ_2	
6D rotation							
para-H_2–CS	$j_1^{max} = 30, j_2 = 0,2$	12	8	18	8	4	$(16, 30, 80, 160)^b$
ortho-H_2–CS	$j_1^{max} = 30, j_2 = 1,3$	12	8	18	8	4	$(18, 32, 82, 162)^b$
6D rovibration							
para-H_2–CS	$[(0,35;1,20)(0,2)]^a$	12	8	18	8	4	$(16, 30, 80, 160)^b$
ortho-H_2–CS	$[(0,35;1,20)(0,3)]^a$	12	8	18	8	4	$(18, 32, 82, 162)^b$

[a] Basis set $\left[\left(v_1 = 0, j_{v_1=0}^{max}; v_1 = 1, j_{v_1=1}^{max}\right)\left(v_2 = 0, j_{v_2=0}^{max}\right)\right]$ is presented by the maximum rotational quantum number $j_{v_1}^{max}$ and $j_{v_2}^{max}$ included in each relevant vibrational level v_1 and v_2 for CS and H_2, respectively. [b] Maximum values of the total angular momentum quantum number $J(J_{E_1}, J_{E_2}, J_{E_3}, J_{E_4})$ used in scattering calculations for collision energies E_1 = 10, E_2 = 100, E_3 = 1000, and E_4 = 3000 cm^{-1}, respectively.

corresponding to the $j_1 = 5 \rightarrow 0$ transition, *i.e.*, the largest $|\Delta j_1 = j_1' - j_1|$. While for collision energies above 200 cm^{-1} the state-to-state quenching cross sections are dominated by $\Delta j_1 = -2$ transitions. Above $\sim$1000 cm^{-1}, the cross sections for $j_1 = 5 \rightarrow 1$ becomes larger than $j_1 = 5 \rightarrow 2$. The agreement between our results and the results of Denis-Alpizar *et al.*[13] is reasonable, though differences are seen in the low collision energy region due to the presence of scattering resonances. These differences tend to disappear as the collision energy is increased. One exception is the transition $j_1 = 5 \rightarrow 0$, where good agreement is only obtained for collision energies between 150 and 500 cm^{-1}, but these cross sections have the smallest magnitude. For *ortho*-H_2, as Fig. 4(b) depicts, the state-to-state cross sections exhibit similar trend as for *para*-H_2. The energy gap law is more pronounced here with a decrease of the cross section with increase in $|\Delta j_1|$. However, the resonance features are almost absent, presumably due to the broader range of partial waves involved. The quenching cross sections are dominated by $\Delta j_1 = -1$ transition for collision energies below $\sim$1000 cm^{-1}, followed by $\Delta j_1 = -2$. Except for the $j_1 = 5 \rightarrow 0$ transition at low collision energies, our results are in very good agreement with the results of Denis-Alpizar *et al.*[13]

Fig. 5(a and b) display the total rotational quenching cross sections from initial states j_1 = 1–5 of CS with *para*-H_2 ($j_2 = 0$) and *ortho*-H_2 ($j_2 = 1$), respectively. It is found that for both *para*-H_2 and *ortho*-H_2, except for collision energies below $\sim$ 3 cm^{-1}, the total rotational quenching cross sections increase with increasing initial j_1. For *para*-H_2, the resonance features observed in the state-to-state cross sections can also be noted in the total quenching cross sections, particularly in the $j_1 = 1$ state.

In Fig. 6, we provide a comparison between the *para*-H_2 and *ortho*-H_2 cross sections for initial rotational states $j_1 = 1$ and 2.

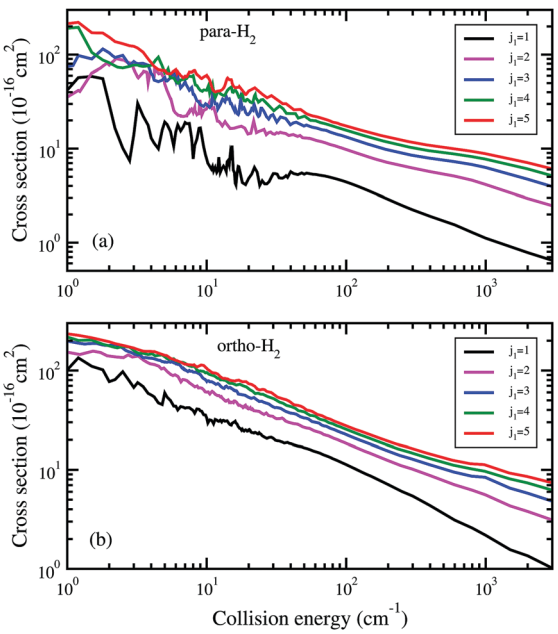

Fig. 5 Total rotational de-excitation cross sections for CS(j_1) from initial states j_1 = 1, 2, 3, 4, and 5. (a) CS in collision with *para*-H_2, $j_2 = j_2' = 0$; (b) CS in collision with *ortho*-H_2, $j_2 = j_2' = 1$.

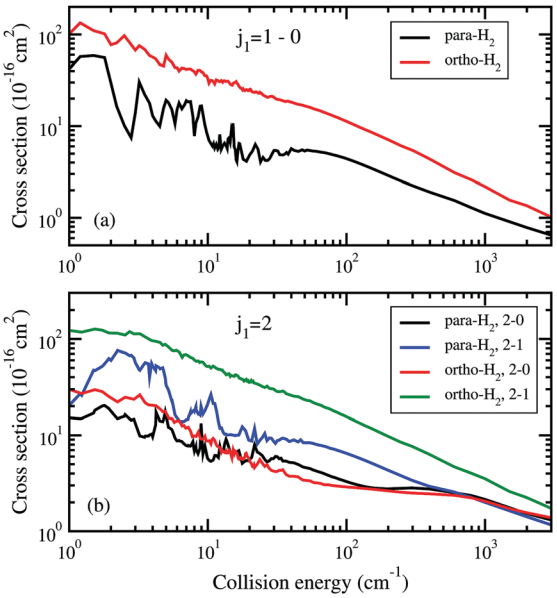

Fig. 6 Comparison of the rotational state-to-state de-excitation cross sections for CS in collision with *para*- and *ortho*-H_2. (a) From initial state $j_1 = 1$; (b) from initial state $j_1 = 2$.

For $\Delta j_1 = -1$, the cross section of *ortho*-H_2 are larger than that of *para*-H_2 over the whole range of collision energy. While for the $j_1 = 2 \rightarrow 0$ transition, the cross sections of *para*-H_2 and *ortho*-H_2 are of comparable magnitude, though the resonance dominated region for *para*-H_2 shows significant differences.

In Fig. 7(a and b) we show the temperature dependence of the rate coefficients for rotational quenching of CS from $j_1 = 2$ induced by *para*- and *ortho*-H_2 collisions, respectively, in the temperatures range of 5 to 600 K. For comparison, the corresponding rate coefficients of Denis-Alpizar *et al.*[14] are also included. The temperature dependence is the steepest for the $j_1 = 2 \rightarrow 0$ rate coefficient for *para*-H_2 collisions. While for $j_1 = 2 \rightarrow 1$, the rate coefficient first decreases with temperature from T = 5–20 K, then increases gradually with increasing temperature. Compared to the results of Denis-Alpizar *et al.*,[14] good agreement is observed for the $j_1 = 2 \rightarrow 0$ rate coefficients. However, for the $j_1 = 2 \rightarrow 1$ transition, our rate coefficient is larger than the results of Denis-Alpizar *et al.* but the differences tend to vanish as the temperature is increased. As shown in Fig. 2, the VCSH2 PES and the PES of Denis-Alpizar *et al.*[20] have different well depths with VCSH2 being the shallower one. This leads to different resonance structures in the cross sections on the two PESs, particularly, at low collision energies. The differences in the rate coefficients at low temperatures may be attributed to the different resonance structures. Fig. 8 provides a comparison of the state-to-state rate coefficients from the present work for $j_1 = 5$ with that of Denis-Alpizar *et al.*.[14] The *para*-H_2 results shown in Fig. 8(a) are in reasonable agreement with the results of Denis-Alpizar *et al.* while the *ortho*-H_2 results presented in Fig. 8(b) are in excellent agreement.

When rate coefficients for a particular collision complex are lacking, it has been argued that rate coefficients from chemically similar systems could be at adopted.[58] We test this idea by comparing the current results from CS to prior work on SiO[36]

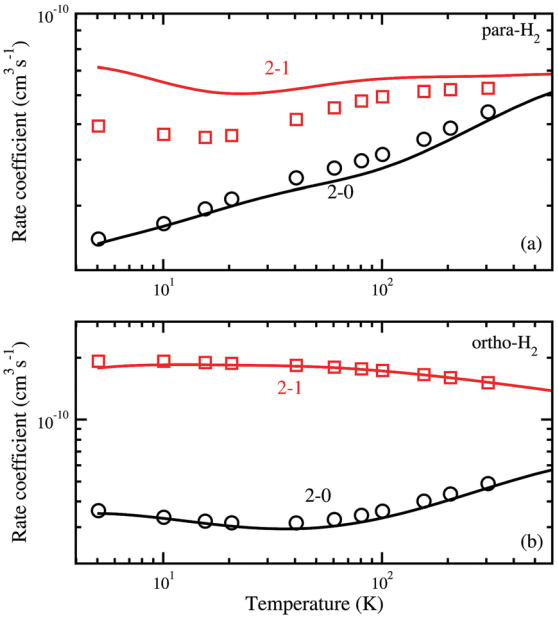

Fig. 7 Rotational state-to-state de-excitation rate coefficients compared with the results of Denis-Alpizar *et al.* (D–A)[14] for CS(j_1 = 2) in collision with (a) *para*-H_2 (j_2 = 0) and (b) *ortho*-H_2 (j_2 = 1).

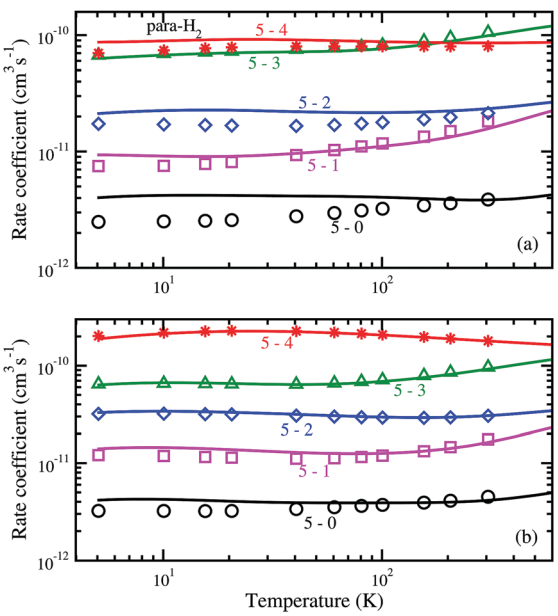

Fig. 8 Rotational state-to-state de-excitation rate coefficients compared with D–A for CS(j_1 = 5) in collision with (a) *para*-H_2(j_2 = 0) and (b) *ortho*-H_2(j_2 = 1).

and SiS.[59,60] In Fig. 9, the state-to-state rate coefficients for rotational quenching from initial state j_1 = 3 for *para*-H_2 collisions are shown. The rate coefficients differ by a factor of ~5 with no clear trend. Adoption of such an approximation is clearly not advisable.

3.2 Vibrational quenching

Here we present close-coupling calculations of rovibrational transitions in CS due to H_2 collisions in full-dimensionality, the main focus of this work.

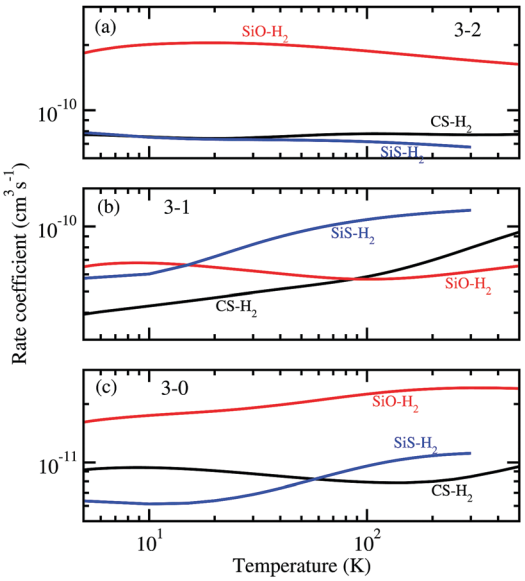

Fig. 9 Rotational state-to-state de-excitation rate coefficients from initial j_1 = 3 of CS, SiO, and SiS in collisions with *para*-H_2(j_2 = 0). (a) j_1 = 3 → 2, (b) j_1 = 3 → 1, (c) j_1 = 3 → 0.

The state-to-state quenching cross sections were computed for CS rovibrational transitions from v_1 = 1, CS(v_1 = 1, j_1) + H_2(v_2 = 0, j_2) → CS(v_1' = 0, j_1') + H_2(v_2' = 0, j_2'), *i.e.*, ($1j_10j_2$) → ($0j_1'0j_2'$). In our calculations, initial j_1 = 0–5 and final j_1' = 0, 1, 2, ⋯, 35. For *para*-H_2, j_2 = 0, j_2' = 0 and 2, while for *ortho*-H_2, j_2 = 1, j_2' = 1 and 3 are considered. We only consider the rotational excitations of H_2 within its ground vibrational state, *i.e.*, v_2 = v_2' = 0 for all of the results presented here. The basis sets employed in the scattering calculations are given in Table 1. All vibrational quenching cross sections were calculated for collision energies between 1 and 3000 cm^{-1}.

As examples, we show in Fig. 10 the state-to-state quenching cross sections from initial CMS (1000) and (1001) into selected final rotational states in v_1' = 0, j_1' = 0, 2, 4, 6, 8, 10, 15, 20, and 25. These results correspond to rotationally elastic scattering of the H_2 molecule, *i.e.*, j_2 = 0 → j_2' = 0. As seen from Fig. 10, for both *para*-H_2 and *ortho*-H_2 colliders, a large number of resonances are observed in the cross sections at collision energies between 1 and 50 cm^{-1}. We also notice that the resonances persist to higher energies with increasing j_1'. Additionally, the state-to-state quenching cross sections increase with collision energy for energies above ~50 cm^{-1}. Overall, the cross sections corresponding to $j_1' \leq 15$ show similar resonance structures and exhibit similar energy dependence. The cross sections for j_1' = 20 and 25 are about two to three orders of magnitude smaller than other transitions for both *para*- and *ortho*-H_2 for collision energies below 300 cm^{-1}, however they increase rapidly with energy, and the cross section of j_1' = 25 becomes the largest at an energy of 3000 cm^{-1}.

Next we discuss the effect of vibrational excitation of CS on its pure rotational quenching. This is provided in Fig. 11 for v_1 = 0 and 1 for rotational levels j_1 = 1 and 5 to all $j_1' < j_1$ for *para*-H_2 with H_2 scattered elastically. It can be seen that the cross sections are nearly identical for v_1 = 0 and 1, over the

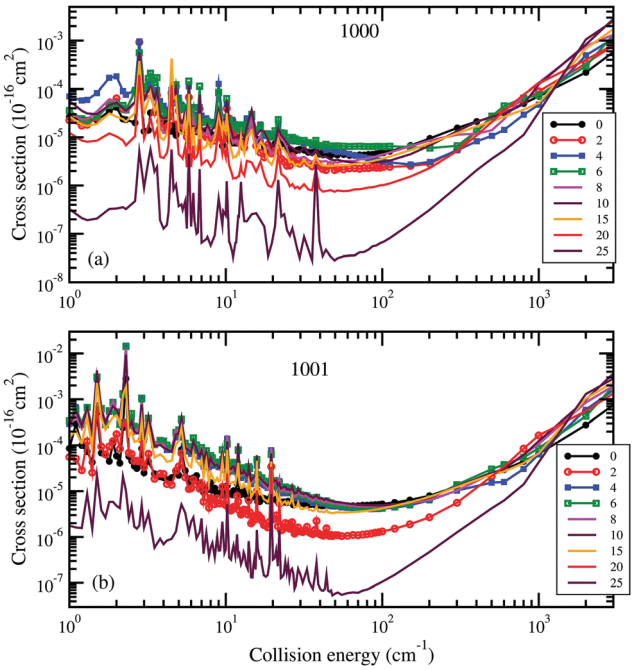

Fig. 10 Vibrational state-to-state quenching cross section for transitions CS(v_1 = 1, j_1 = 0) + H_2(j_2) → CS(v_1' = 0, j_1') + H_2(j_2), j_1' = 0, 2, 4, 6, 8, 10, 15, 20, and 25. (a) *para*-H_2(j_2 = 0) and (b) *ortho*-H_2(j_2 = 1).

whole range of energies considered in this work demonstrating the negligible effect of vibrational excitation of CS on pure rotational quenching. This is due to the almost harmonic nature of the v = 0 and 1 vibrational levels of CS. Similar results are found for *ortho*-H_2 collisions. This also means that, effect of vibrational excitation of CS can be ignored for pure rotational transitions in CS in collisions with *ortho*- and *para*-H_2, at least for low vibrational levels. A similar conclusion was also drawn for the SiO–H_2 system.[36]

Using eqn (7) the total vibrational quenching cross section of CS from initial CMS (1000) and (1001) was obtained by summing the state to state quenching cross sections over the final rotational state j_1' of CS in vibrational state v_1 = 0. These total quenching cross section were calculated for elastic and inelastic transitions in H_2.

Fig. 12(a) presents the energy dependence of the total v_1 = 1 → v_1' = 0 quenching cross section with *para*-H_2 from CMSs (1000) for elastic (j_2 = 0 → j_2' = 0) and inelastic (j_2 = 0 → j_2' = 2) transitions in H_2. While they exhibit similar energy dependencies and similar resonance structures at low energies, the cross sections for elastic transition in H_2 are about a factor of two larger than its inelastic counterpart in the entire energy range. For *ortho*-H_2 and initial CMS (1001), Fig. 12(b) shows that the total vibrational quenching cross sections for elastic (j_2 = 1 → j_2' = 1) and inelastic (j_2 = 1 → j_2' = 3) transitions in H_2 are comparable for collision energies below ∼200 cm^{-1}. For energies above ∼200 cm^{-1}, the cross section for H_2 rotation preserving transition becomes increasingly dominant.

We also calculated the state-to-state and total vibrational quenching rate coefficients of CS(v_1 = 1, j_1) in collisions with *para*-H_2 (j_2 = 0) and *ortho*-H_2 (j_2 = 1) for j_1 = 0–5. State-to-state rate coefficients are obtained for j_1' = 0, 1, 2,⋯, 35 and j_2' = 0 and 2 for *para*-H_2 and j_2' = 1 and 3 for *ortho*-H_2. Unfortunately, there are no published experimental or theoretical state-to-state rate coefficients available for comparison. As an example, in Fig. 13 we show the total vibrational quenching rate coefficients for temperatures between 1 and 600 K for CMS (1000) to (v_1' = 0) and j_2' = 0, and CMS (1001) to (v_1' = 0) and j_2' = 1.

Previously we have provided a comparison of CS–H_2 rate coefficients with that of CO–H_2 (ref. 33) and for SiO–H_2 (ref. 36). It was shown that for the same transitions, the total quenching rate coefficients of CO–H_2 are typically ∼2–3 orders of magnitude smaller than that of CS–H_2 and SiO–H_2. The large magnitude of SiO–H_2 rate coefficients are likely due to the high anisotropy of the SiO–H_2 PES. Interestingly, at high temperatures the CS–H_2 rate coefficients merge with those of SiO–H_2. Furthermore, generally the rate coefficients increase with increasing well depth of the interaction PES, the SiO–H_2 rate coefficients are largest with a well depth of 293.2 cm^{-1} and CO–H_2 rate coefficients are smallest with a well depth of 93.1 cm^{-1}.

4 Astrophysical applications

A quantitative non-LTE modeling of molecular excitation and line formation processes from infrared and submillimetre observations requires detailed knowledge of collisional rate coefficients for transitions between the rovibrational states of molecules over a wide range of levels and temperatures. Molecular collisions, which are responsible for most of the excitation and reaction processes, are important in the interstellar medium (ISM). Particularly, in cold molecular clouds, collisional processes are the dominant factor in analysis of emission and absorption spectra, and H_2 and He are the most important collision partners due to their large abundances, except in photodissociation regions (PDRs) and diffuse gas where collisions with electrons and H can become important. However, direct measurements of the collisional rate coefficients are difficulty and complicated; astrophysical modeling heavily rely on theoretical calculations.[61]

Carbon monosulfide and its isotopic species have been detected in a large range of astrophysical environments. As a high-density tracer of dense gas, CS emission is normally used in the study of star forming regions. Using the IRAM Plateau de Bure interferometer Guilloteau *et al.*[62] observed two CS transitions j_1 = 3–2 and j_1 = 5–4 in the DM Tau disk. The line intensities were used to determine the magnitude of the turbulent motions in the outer parts of the disk. Maxted *et al.*[63] detected emission j_1 = 1–0 and j_1 = 2–1 of CS and its isotopologues in four of the densest cores towards the western rim of supernova remnant RX J1713.7-3946 and confirmed the presence of dense gas ≥10^4 cm^{-3} in the region. More recently, CS emission (1–0) was used in the investigation of the nature of the supernova remnant HESS J1731-347.[64] Line emission from rotational transition j_1 = 7–6 within the vibrationally excited state v = 1 was observed in IRAS 16293-2422.[65] Gómez-Ruiz *et al.*[66] detected CS and isotopologues

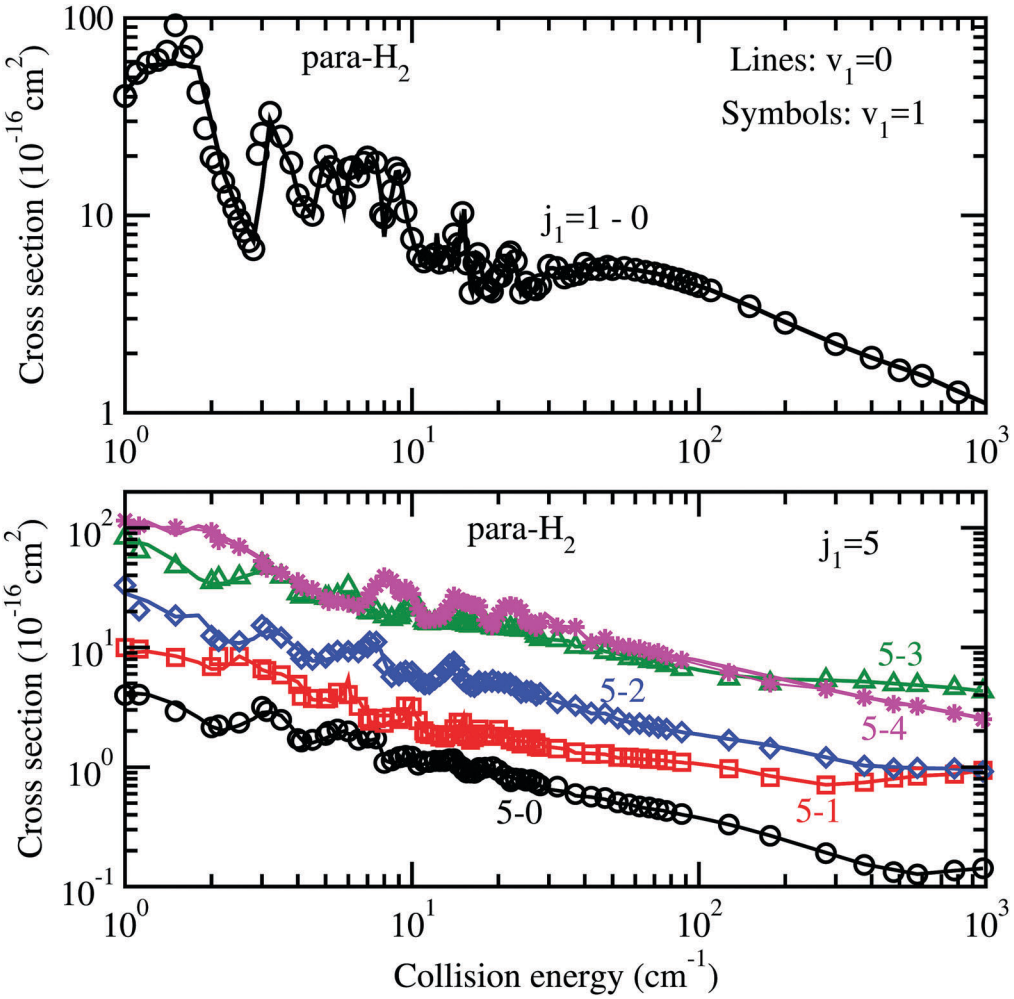

Fig. 11 Rotational quenching state-to-state excitation cross section of CS from initial states j_1 = 1 and 5 to j_1', $j_1' < j_1$. (a) and (b): *para*-H_2. For each transition, the comparison is made between v_1 = 0 and v_1 = 1.

$^{12}C^{32}S$, $^{12}C^{34}S$, $^{13}C^{32}S$, $^{12}C^{33}S$, for a total of 18 transitions with Herschel/HIFI and IRAM-30m at L1157-B1. With Herschel/HIFI spectral line survey[67] CS transitions were detected toward the Orion Bar, tracing the warm and dense gas with temperatures of 100–150 K and densities of 10^5–10^6 cm^{-3}. NLTE analysis was also performed with RADEX, where the CS–H_2 rate coefficients were obtained by reduced-mass scaling the rate coefficients with He of Lique *et al.*[21] Using the IRAM 30 m telescope, Aladro *et al.*[68] performed a molecular line survey towards the circumnuclear regions of eight active galaxies, CS and its isotopologues were identified in M83, M82, M51, and NGC 253. Using the Atacama Large Millimeter/submillimeter Array (ALMA), Takano *et al.*[69] performed a high resolution imaging study of molecular lines near the supermassive black hole at the center of galaxy NGC 1068. CS emission of j_1 = 2–1 was distributed both in the circumnuclear disk and the starburst ring. Walter *et al.*[70] investigated dense molecular gas tracers in the nearby starburst galaxy NGC 253 using ALMA, CS(j_1 = 2–1) was detected in the molecular outflow.

Vibrationally excited molecules, which are excited by collision or infrared radiation, can be used to probe extreme physical conditions with high gas densities and temperatures. The first observation of vibrationally excited CS in the circumstellar shell of IRC + 10216 was reported by Turner[71] through transitions j_1 = 2 → 1 and 5 → 4 in v_1 = 1. In 2000, Highberger *et al.*[72] reobserved these lines and also detected new transitions of j_1 = 3–2, 6–5, and 7–6 of vibrationally excited CS(v = 1) toward IRC + 10216. Using Submillimeter Array, Patel *et al.*[73] detected the CS v_1 = 2, j_1 = 7–6 transition from the inner envelope of IRC + 10216. Finally, vibrational absorption lines for CS have been detected for its fundamental band near 8 μm in IRC + 10216.[74] These observations used the Texas Echelon-cross-Eschelle Spectrograph (TEXES) on the 3 m Infrared Telescope facility.

Our present full-dimensional scattering calculation will be able to provide accurate rovibrational state-to-state CS–H_2 collisional data for future modeling of protostars, the infrared sources discussed above, and future FIR and submillimeter observations with Herschel and ALMA. Furthermore, CS vibrational bands in the 1–5 μm region will be accessible by the James Webb Space Telescope (JWST) to be launched in 2021 and currently with SOFIA using the EXES (5–28 μm) or FORCAST (5–40 μm) instruments. In PPDs, CS vibrational lines probe the inner warm regions which are exposed to the UV radiation from the protostar.

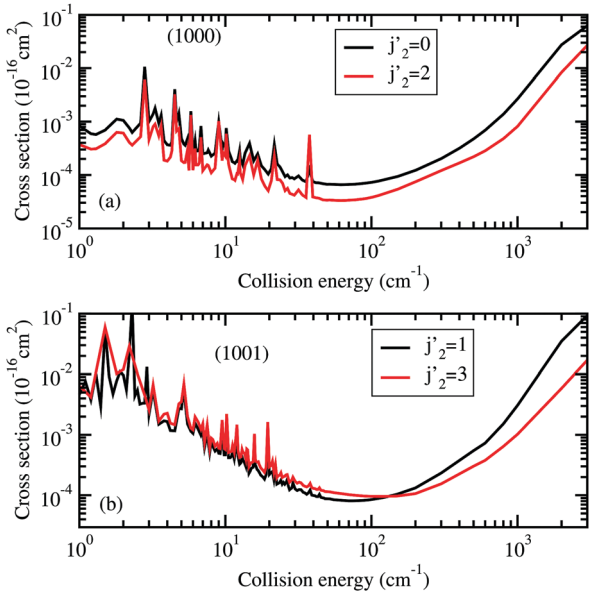

Fig. 12 Total vibrational quenching cross section for transitions CS(v_1 = 1, j_1) + H_2(j_2) → CS(v_1' = 0) + H_2(j_2). j_1 = 0. (a) *para*-H_2 (j_2 = 0). (b) *ortho*-H_2 (j_2 = 1).

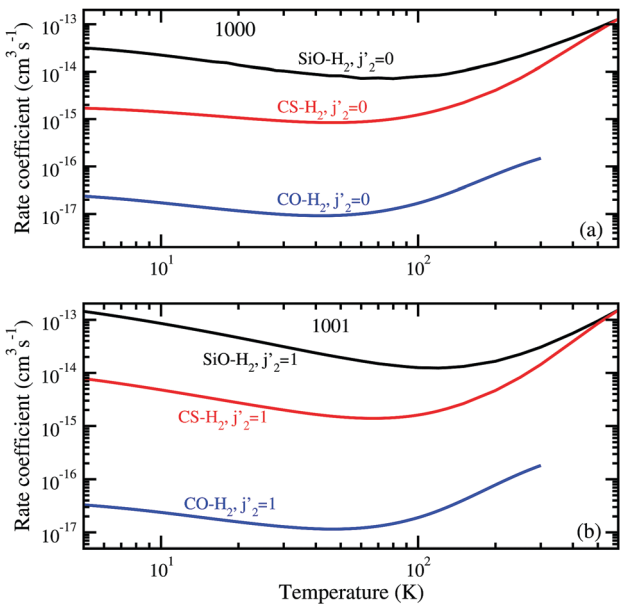

Fig. 13 Total rate coefficients for the vibrational quenching of CS compared to the same transitions for CO from ref. 33 and SiO from ref. 33. (a) from (1000) to v_1' = 0 + *para*-H_2(v_2' = 0, j_2' = 0). (b) From (1001) to v_1' = 0 + *ortho*-H_2(v_2' = 0, j_2' = 1).

5 Summary

We constructed a 6-dimensional potential energy surface for CS–H_2 based on high-level electronic structure calculations. State-to-state cross sections for rotational and rovibrational transitions in CS in collisions with H_2 are reported using full-dimensional quantum scattering calculations and an analytical fit of the potential surface.

Cross sections and rate coefficients for pure rotational transitions from the present study are found to be in good agreement with the rigid-rotor approximation calculations of Denis-Alpizar *et al.*[13,14] using a 4-dimensional potential surface. The vibrational quenching cross sections and rate coefficients have been reported for the first time. In future work, we plan to extend the current calculations to higher rotational and vibrational states of CS and include the effect of vibrational excitation of the H_2 molecule.

Conflicts of interest

There are no conflicts of interest to declare.

Acknowledgements

Work at UGA and Emory was supported by NASA grant NNX16AF09G, at UNLV by NSF Grant No. PHY-1505557, and at Penn State by NSF Grant No. PHY-1503615. This study was supported in part by resources and technical expertise from the UGA Georgia Advanced Computing Resource Center (GACRC), and UNLV National Supercomputing Institute & Dedicated Research Network. We thank Shan-Ho Tsai (GACRC), Jeff Deroshia (UGA Department of Physics and Astronomy), and Ron Young (UNLV) for computational assistance.

References

1 D. Flower, *Molecular Collisions in the Interstellar Medium*, Cambridge University Press, Cambrdige, 2nd edn, 2011.
2 A. A. Penzias, P. M. Solomon, R. W. Wilson and K. B. Jefferts, *Astrophys. J.*, 1971, **168**, L53–L58.
3 R. W. Wilson, A. A. Penzias, P. G. Wannier and R. A. Linke, *Astrophys. J.*, 1976, **204**, L135–L137.
4 K. S. K. Swamy, *Astron. Astrophys.*, 1981, **97**, 110.
5 H. A. Thronson Jr. and C. J. Lada, *Astrophys. J.*, 1984, **284**, 135.
6 K. S. Noll, M. A. McGrath, L. M. Trafton, S. K. Atreya, J. J. Caldwell, H. A. Weaver, R. V. Yelle, C. Barnet and S. Edgington, *Science*, 1995, **267**, 1307–1313.
7 D. P. Ruffle, T. W. Hartquist, P. Caselli and D. A. Williams, *Mon. Not. R. Astron. Soc.*, 1999, **306**, 691–695.
8 D. A. Neufeld, B. Godard and M. Gerin, *et al.*, *Astron. Astrophys.*, 2015, **577**, A49.
9 R. Moreno, E. Lellouch and T. Cavalie, *et al.*, *Astron. Astrophys.*, 2017, **608**, L5.
10 C. Vastel, D. Quénard and R. Le Gal, *et al.*, *Mon. Not. R. Astron. Soc.*, 2018, **478**, 5519–5537.
11 S. Green and S. Chapmen, *Astrophys. J., Suppl. Ser.*, 1978, **37**, 169–194.
12 B. E. Turner, K.-W. Chan, S. Green and D. A. Lubowich, *Astrophys. J.*, 1992, **399**, 114–133.
13 O. Denis-Alpizar, T. Stoecklin, P. Halvick and M.-L. Dubernet, *J. Chem. Phys.*, 2013, **139**, 204304.
14 O. Denis-Alpizar, T. Stoecklin, S. Guilloteau and A. Dutrey, *Mon. Not. R. Astron. Soc.*, 2018, **478**, 1811–1817.

15 R. G. Gordon and J. S. Kim, *J. Chem. Phys.*, 1972, **56**, 3122–3133.
16 M. A. Albrecht, *Astron. Astrophys.*, 1983, **127**, 409–410.
17 J. H. Bieging, L. B. G. Knee, W. B. Latter and H. Olofsson, *Astron. Astrophys.*, 1998, **339**, 811–821.
18 K. T. Wong, T. Kamiński, K. M. Menten and F. Wyrowski, *Astron. Astrophys.*, 2016, **590**, A127.
19 G. Guillon, T. Stoecklin, A. Voronin and P. Halvick, *J. Chem. Phys.*, 2008, **129**, 104308.
20 O. Denis-Alpizar, T. Stoecklin, P. Halvick, M.-L. Dubernet and S. Marinakis, *J. Chem. Phys.*, 2012, **137**, 234301.
21 F. Lique, A. Spielfiedel and J. Cernicharo, *Astron. Astrophys.*, 2006, **451**, 1125–1132.
22 F. Lique and A. Spielfiedel, *Astron. Astrophys.*, 2007, **451**, 1179–1185.
23 F. L. Schöier, F. F. S. van der Tak, E. F. van Dishoeck and J. H. Black, *Astron. Astrophys.*, 2005, **432**, 369–379.
24 I. W. M. Smith, *Trans. Faraday Soc.*, 1968, **64**, 3183–3191.
25 C. Morley and I. W. M. Smith, *Trans. Faraday Soc.*, 1971, **67**, 2575–2585.
26 K. Takayanagi, *Adv. At. Mol. Phys.*, 1965, **1**, 149–194.
27 S. K. Pogrebnya and D. C. Clary, *Chem. Phys. Lett.*, 2002, **363**, 523–528.
28 R. V. Krems, *TwoBC – quantum scattering program*, University of British Columbia, Vancouver, Canada, 2006.
29 G. Quéméner, N. Balakrishnan and R. V. Krems, *Phys. Rev. A: At., Mol., Opt. Phys.*, 2008, **77**, 030704.
30 G. Quéméner and N. Balakrishnan, *J. Chem. Phys.*, 2009, **130**, 114303.
31 S. F. dos Santos, N. Balakrishnan, S. Lepp, G. Quéméner, R. C. Forrey, R. J. Hinde and P. C. Stancil, *J. Chem. Phys.*, 2011, **134**, 214303.
32 S. F. dos Santos, N. Balakrishnan, R. C. Forrey and P. C. Stancil, *J. Chem. Phys.*, 2013, **138**, 104302.
33 B. H. Yang, P. Zhang, X. Wang, P. C. Stancil, J. M. Bowman, N. Balakrishnan and R. C. Forrey, *Nat. Commun.*, 2015, **6**, 6629.
34 B. H. Yang, N. Balakrishnan, P. Zhang, X. Wang, J. M. Bowman, R. C. Forrey and P. C. Stancil, *J. Chem. Phys.*, 2016, **145**, 034308.
35 B. H. Yang, X. Wang, P. C. Stancil, J. M. Bowman, N. Balakrishnan and R. C. Forrey, *J. Chem. Phys.*, 2016, **145**, 224307.
36 B. H. Yang, P. Zhang, X. H. Wang, P. C. Stancil, J. M. Bowman, N. Balakrishnan, B. M. McLaughlin and R. C. Forrey, *J. Phys. Chem. A*, 2018, **122**, 1511–1520.
37 R. C. Forrey, B. H. Yang, P. C. Stancil and N. Balakrishnan, *Chem. Phys.*, 2015, **462**, 71–78.
38 C. Castro, K. Doan, M. Klemka, R. C. Forrey, B. H. Yang, P. C. Stancil and N. Balakrishnan, *Mol. Astrophys.*, 2017, **6**, 47–58.
39 H. Burton, R. Mysliwiec, R. C. Forrey, B. H. Yang, P. C. Stancil and N. Balakrishnan, *Mol. Astrophys.*, 2017, **11**, 23–32.
40 B. J. Braams and J. M. Bowman, *Int. Rev. Phys. Chem.*, 2009, **28**, 577–606.
41 H.-J. Werner, P. J. Knowles, G. Knizia, F. R. Manby and M. Schütz, *WIREs Comput. Mol. Sci.*, 2012, **2**, 242–253.
42 H.-J. Werner, P. J. Knowles, G. Knizia, F. R. Manby, M. Schütz and P. Celani *et al.*, *MOLPRO, version 2012.1, a package of ab initio programs*, 2012, http://www.molpro.net.
43 T. B. Adler, G. Knizia and H.-J. Werner, *J. Chem. Phys.*, 2007, **127**, 221106.
44 H.-J. Werner, T. B. Adler and F. R. Manby, *J. Chem. Phys.*, 2007, **126**, 164102.
45 T. H. Dunning Jr., *J. Chem. Phys.*, 1989, **90**, 1007–1023.
46 T. H. Dunning Jr., K. A. Peterson and A. K. Wilson, *J. Chem. Phys.*, 2001, **114**, 9244–9253.
47 F. Weigend, A. Köhn and C. Hättig, *J. Chem. Phys.*, 2002, **116**, 3175–3183.
48 C. Hättig, *Phys. Chem. Chem. Phys.*, 2005, **7**, 59–66.
49 EMSL basis set exchange, https://bse.pnl.gov/bse/portal.
50 D. Feller, K. A. Peterson and J. G. Hill, *J. Chem. Phys.*, 2010, **133**, 184102.
51 S. F. Boys and F. Bernardi, *Mol. Phys.*, 1970, **19**, 553–566.
52 J. M. Bowman, B. J. Braams and S. Carter, *et al.*, *J. Phys. Chem. Lett.*, 2010, **1**, 1866–1874.
53 Z. Xie and J. M. Bowman, *J. Chem. Theory Comput.*, 2010, **6**, 26–34, see https://scholarblogs.emory.edu/bowman/msa/.
54 S. Green, *J. Chem. Phys.*, 1975, **62**, 2271–2277.
55 B. R. Johnson, *J. Comp. Physiol.*, 1973, **13**, 445–449.
56 G. Paulose, E. J. Barton, S. N. Yurchenko and J. Tennyson, *Mon. Not. R. Astron. Soc.*, 2013, **454**, 1931–1939.
57 D. W. Schwenke, *J. Chem. Phys.*, 1988, **89**, 2076–2091.
58 F. van der Tak, From The Molecular Universe, *Proc. IAU Symp.*, ed. J. Cernicharo and R. Bachiller, 2011, p. 280.
59 F. Lique and J. Kłos, *J. Chem. Phys.*, 2008, **128**, 034306.
60 J. Kłos and F. Lique, *Mon. Not. R. Astron. Soc.*, 2008, **390**, 239–244.
61 E. Roueff and F. Lique, *Chem. Rev.*, 2013, **113**, 8906–8938.
62 S. Guilloteau, A. Dutrey, V. Wakelam, F. Hersant, D. Semenov, E. Chapillon, T. Henning and V. Piétu, *Astron. Astrophys.*, 2012, **548**, A70.
63 N. I. Maxted, G. P. Rowell and B. R. Dawson, *et al.*, *Mon. Not. R. Astron. Soc.*, 2012, **422**, 2230–2245.
64 N. Maxted, M. Burton and C. Braiding, *et al.*, *Mon. Not. R. Astron. Soc.*, 2018, **474**, 662–676.
65 G. A. Blake, E. F. van Dishoeck, D. J. Jansen, T. D. Groesbeck and L. G. Mundy, *Astrophys. J.*, 1994, **428**, 680–692.
66 A. I. Gómez-Ruiz, C. Codella, B. Lefloch, M. Benedettini, G. Busquet, C. Ceccarelli, B. Nisini, L. Podio and S. Viti, *Mon. Not. R. Astron. Soc.*, 2014, **446**, 3346–3355.
67 Z. Nagy, Y. Choi and V. Ossenkopf-Okada, *et al.*, *Astron. Astrophys.*, 2017, **599**, A22.
68 R. Aladro, S. Martín, D. Riquelme and C. Henkel, *et al.*, *Astron. Astraphys.*, 2015, **579**, A101.
69 S. Takano, T. Nakajima and K. Kohno, *et al.*, *Publ. Astron. Soc. Jpn.*, 2014, **66**, 75.
70 F. Walter, A. D. Bolatto and A. K. Leroy, *et al.*, *Astrophys. J.*, 2017, **835**, 265.
71 B. E. Turner, *Astron. Astrophys.*, 1987, **182**, L15–L18.
72 J. L. Highberger, A. J. Apponi, J. H. Bieging, L. M. Ziyrys and J. G. Mangun, *Astrophys. J.*, 2000, **544**, 881–888.
73 N. A. Patel, K. H. Young and S. Brünken, *et al.*, *Astrophys. J.*, 2009, **692**, 1205–1210.
74 J. P. Fonfría, M. Agúndez, J. Cernicharo, M. J. Richter and J. H. Lacy, *Astrophys. J.*, 2018, **852**, 80.

